Available online at www.sciencedirect.com
SCIENCE DIRECT®
Journal of Solid State Chemistry 176 (2003) 390–399
JOURNAL OF SOLID STATE CHEMISTRY
http://elsevier.com/locate/jssc

Electronic structure, chemical bonding, and spin polarization in ferromagnetic MnAl

Yasemin Kurtulus and Richard Dronskowski*

Institut für Anorganische Chemie, Rheinisch-Westfälische Technische Hochschule, Prof.-Pirlet-Str. 1, D–52056 Aachen, Germany

Received 23 January 2003; received in revised form 14 April 2003; accepted 25 April 2003

Abstract

The electronic structure of ferromagnetic τ-MnAl has been calculated using density-functional techniques (TB-LMTO-ASA, FLAPW) and quantum-chemically analyzed by means of the crystal orbital Hamilton population tool. While all observable quantities are in good agreement with experiment, the tetragonal structure of ferromagnetic MnAl is interpreted to arise from a nonmagnetic cubic structure by two subsequent steps, namely (a) an electronic distortion due to spin polarization followed by (b) a structural distortion into the tetragonal system. The various strengths of interatomic bonding have been calculated in order to elucidate the competition between electronic and structural distortion.

Keywords: τ-MnAl; Ferromagnetism; DFT calculations; Jahn–Teller distortion; COHP; Spin polarization

1. Introduction

The binary system Mn/Al is extraordinarily rich in phases; up to now, at least 17 of these have been described [1]. Among them, those alloys containing about 50–60 atomic percent of Mn are especially important from the physical point of view. For example, the ferromagnetic τ-phase in the MnAl system, first reported by Kono [2] and Koch et al. [3], can be used as a permanent magnetic material. This τ-phase is an ordered alloy and a strong ferromagnet with $T_C = 653$ K [2], a manganese moment of 1.94 μ_B [4] and an enhanced magnetic anisotropy [3], which is somewhat unusual for compounds without rare earth ions.

Fig. 1 (top) shows the crystal structure of the τ-phase, adopting the AuCu structure type. The face-centered cell can also be described using a primitive tetragonal unit cell denoted with dashed lines. The primitive lattice constants are $\bar{a} = 2.77$ Å and $c = 3.54$ Å, and the tetragonal cell itself can be regarded as being a distorted cubic cell (Fig. 1, bottom). In the following, we will describe both tetragonal and cubic cells exclusively in terms of their reduced cells, and we will therefore shorten the notation by simply writing $\bar{a} = a$.

The alloy τ-MnAl can be prepared from its high-temperature phase, hexagonal close-packed ε-MnAl. The synthesis starts by casting, grinding or milling [5] the metal powders in the appropriate composition followed by annealing at 850 °C and above. The high-temperature ε-phase thus formed is rapidly quenched and then isothermally annealed at temperatures between 400 and 700 °C; this induces first the transformation to the nonmagnetic orthorhombic ε′-phase by an ordering reaction and then to the ferromagnetic, metastable τ-phase by a martensitic transformation [6,7].

In 1994 Sakuma [8] showed, by means of electronic structure calculations, that the magnetocrystalline anisotropy energy of τ-MnAl depends on the axial ratio c/a and that a tetragonal distortion from a cubic structure stabilizes the system in terms of a Jahn–Teller effect. The present work intends to further investigate the Jahn–Teller scenario found in MnAl by including the spin degrees of freedom. In order to do so, total energy calculations (nonmagnetic and magnetic) as a function of the axial ratio c/a were performed, and the band structures and densities of states belonging to both cubic and tetragonal structures were thoroughly analyzed. In addition, the chemical bonding of τ-MnAl upon

*Corresponding author. Fax: 0241-8888-288.
E-mail address: drons@HAL9000.ac.rwth-aachen.de (R. Dronskowski).

0022-4596/03/$ - see front matter © 2003 Elsevier Inc. All rights reserved.
doi:10.1016/S0022-4596(03)00242-1

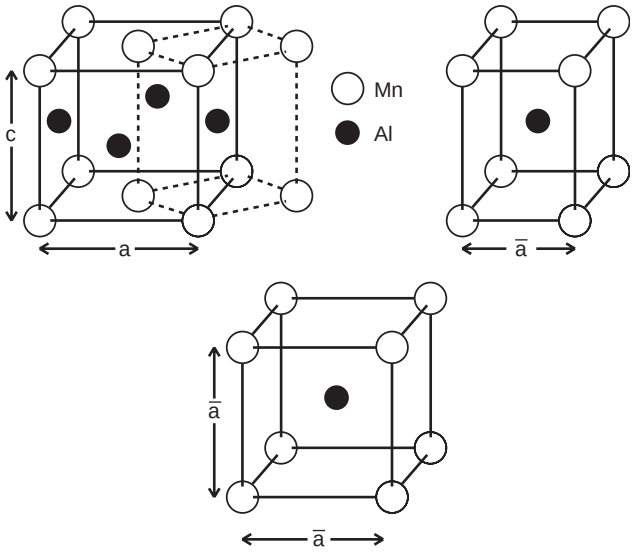

Fig. 1. Top: Crystal structure of τ-MnAl. The dashed lines denote the reduced tetragonal cell, and the tetragonal lattice parameter $\bar{a}$ equals $\frac{a}{2}\sqrt{2}$. Bottom: Idealized simple cubic structure of MnAl.

structural and electronic/magnetic distortion was investigated by means of the crystal orbital hamilton population (COHP) method.

2. Theoretical methodology

Electronic structure calculations on both phases (cubic and tetragonal) were performed using the linear muffin-tin orbital (LMTO) method [9–11] in its tight-binding representation [12]; it represents a fast, linearized form of the Korringa-Kohn-Rostoker (KKR) method [13,14]. LMTO theory accounts for the potential from all the electrons and is applicable to materials composed of atoms from any part of the periodic table. The program used was TB-LMTO-ASA 4.7 [15] with a scalar-relativistic Hamiltonian. Electronic energies were calculated via density-functional theory (DFT), taking the von Barth and Hedin parameterization of the local spin density approximation (LSDA) [16]. Furthermore, a series of total energy calculations was made using the full-potential linearized augmented-plane-wave (FLAPW) method [17] including the generalized gradient approximation (GGA) [18] within the program package WIEN97 [19]. For valence states a scalar-relativistic treatment was included, and core states were treated fully relativistically.

The chemical bonding was investigated using COHP analysis [20]. This technique provides information analogous to the familiar crystal orbital overlap population (COOP) analysis [21] used in extended Hückel calculations [22]. While COOP curves are energy-resolved plots of the Mulliken overlap population between two atoms or orbitals, a COHP curve is an energy-resolved plot of the contribution of a given bond to the bonding energy of the system. There is one very important difference between COHP and COOP curves: while COOPs are usually presented as an *average* of several bonds, COHPs typically include the *sum* of those bonds. While this does not affect the shape of COHP curves, it does change their size. All COHP curves are presented here in a format similar to COOP curves: positive values are bonding, and negative antibonding (i.e., we are plotting −COHP instead of COHP).

Recently, the COHP tool has been used to detect electronic instabilities within the transition metals and their alloys, and these instabilities show up from populated M–M antibonding states in nonmagnetic band structure calculations. When switching from a nonmagnetic (nonspin-polarized) calculation to a magnetic (spin-polarized) one, there results a removal of antibonding states at ε_F for itinerant ferromagnets; in addition, the chemical bonds strengthen within the pure metals [23]. Thus, it has proven possible to rephrase itinerant ferromagnetism (as well as itinerant antiferromagnetism [24]) as an effect arising from chemical bonding itself. By doing so, new ferromagnetic as well as antiferromagnetic alloys were predicted and, eventually, synthesized [25].

The chemical hardness η [26] of a metal (alloy) may serve as another, yet less reliable indicator for the appearance of ferromagnetism. It was shown that ferromagnetic metals and alloys exhibit a characteristic chemical hardness $\eta < 0.2$ eV in their nonmagnetic forms [23] and show a substantial increase of η upon spin polarization. Using Eq. (1) we can determine the chemical hardness η of a metal from the slope of a plot of $\varepsilon_F(N)$ versus N (the number of electrons) at $N = N_0$ (number of valence electrons in the neutral system at fixed nuclear potential) [23]:

$$\eta = \frac{1}{2}\left(\frac{\partial \varepsilon_F}{\partial N}\right)_{V,N_0}. \quad (1)$$

3. Results and discussion

We start our analysis by a series of nonmagnetic (local density approximation, LDA) total energy calculations by use of the TB-LMTO-ASA method in order to find the reason for the tetragonal (as opposed to cubic) structure of MnAl. These calculations were performed for varying c/a ratios for the lattice parameters but keeping with a constant cell volume. The result is plotted in the left part of Fig. 2, showing the minimum energy being very close to $c/a = 1$; thus, nonmagnetic MnAl should be expected to (almost) crystallize in the cubic system!

Since ASA calculations, however, are known to deliver questionable results upon structural deforma-

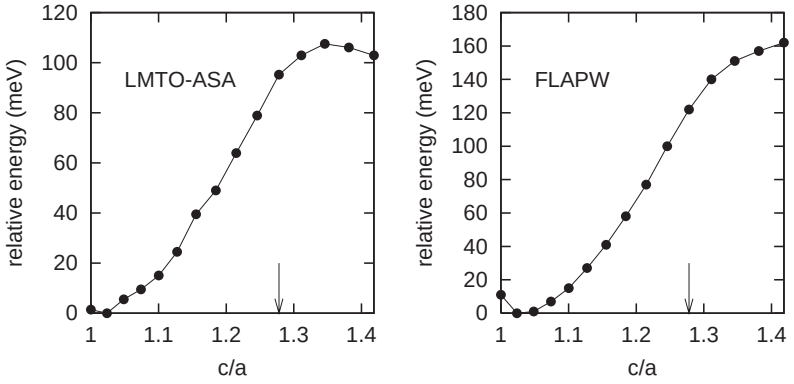

Fig. 2. The total energy of the TB-LMTO-ASA (left) and FLAPW (right) nonmagnetic LDA calculations as a function of the axial ratio c/a. The arrows indicate the experimentally found c/a ratio.

tions because of the underlying shape approximations for the atomic potentials, the series of calculations was repeated using the FLAPW method; these results are given in the right part of Fig. 2. Although there is a small difference in numbers, the qualitative result is the same: nonmagnetic MnAl should adopt a cubic (CsCl-like) structure.

For this cubic structure with a lattice parameter of 3.006 Å, the calculated LMTO atomic charges arrive at −0.194 for Mn and +0.194 for Al. The absolute values, being somewhat dependent on the chosen atomic spheres, should not be overinterpreted, but the trend in charge transfer nicely agrees with what would have been predicted on the basis of absolute electronegativities [26]. The LMTO band structure and density of states (DOS) is shown in Fig. 3. There is an *s*-like band visible in the lower half of the valence region plus five *d*-like bands above. The latter is grouped into a three (Fermi energy region) above two (below) splitting. A moment reflection reveals that the two groups arise because of a t_{2g} above e_g symmetry splitting, schematically depicted in Fig. 4; we stress that this splitting is *reversed* compared to the one found in the elemental 3*d* ferromagnets.

The difference in dispersion of the *d* bands in Fig. 3 is easily understood by refering to the orbital icons in Fig. 4; because of the e_g-set orbitals (d_{z^2}, $d_{x^2-y^2}$) pointing into the internuclear (Mn–Mn) direction and generating σ interactions, it is these orbitals which show a greater dispersion and lie lower in energy. The t_{2g} set (d_{xy}, d_{xz}, d_{yz}), on the other side, is more weakly interacting (π-like), and it is positioned in the frontier band regime. It is here where the total DOS (see right part of Fig. 3) is almost completely dominated by a Mn *d*-character. Other *l* channels (Al-*s*, *p*; Mn-*s*, *p*) can be found below and above the region of the Fermi level.

The DOS at the Fermi level is considerably large; we reiterate, however, that the nonmagnetic total energy calculations *exclude* the possibility of a structural deformation into the tetragonal system. To gain more

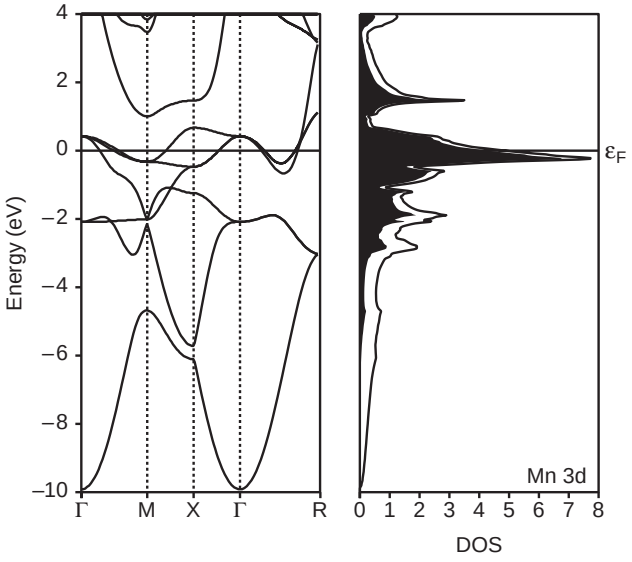

Fig. 3. TB-LMTO-ASA band structure (left) and density of states (right) of MnAl in the cubic structure. The shaded region in the DOS curve corresponds to the projected DOS of the Mn 3*d* orbitals. All curves have been shifted in energy so that ε_F lies at 0.0 eV.

insight into the various interactions, we turn the reader to Fig. 5, offering the COHP analysis of the Mn–Mn, Mn–Al, and Al–Al bonds. For the sake of completeness, the numerical values of the energy-integrated COHPs (denoted ICOHPs) are tabulated in Table 1.

To start with, the strongest bonding interactions (Mn–Al, middle figure) are bonding throughout the occupied bonds and almost perfectly adjusted with respect to the Fermi level; as it seems, a further slight electronic enrichment would stabilize Mn–Al even more. Al–Al interactions (right part of the figure) are weaker in general, and there are even some antibonding states filled just below the Fermi level. When it comes to the Mn–Mn bonds, however, it is interesting to note that, besides the bonding interactions below the Fermi level, there are populated *antibonding* interactions exactly located at ε_F, and it is these destabilizing effects which

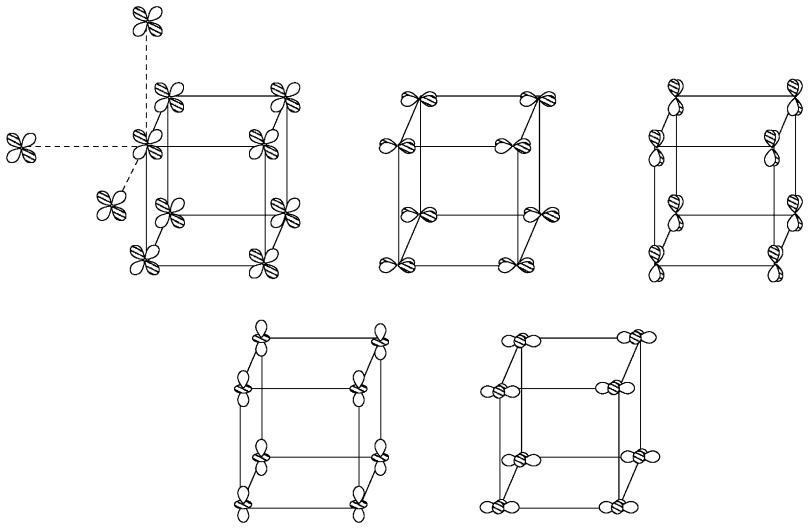

Fig. 4. Representation of the Mn d orbitals of cubic MnAl at the high-symmetry point Γ. The dotted lines in the upper sketch (left) denote the nearest neighbor contacts around each Mn.

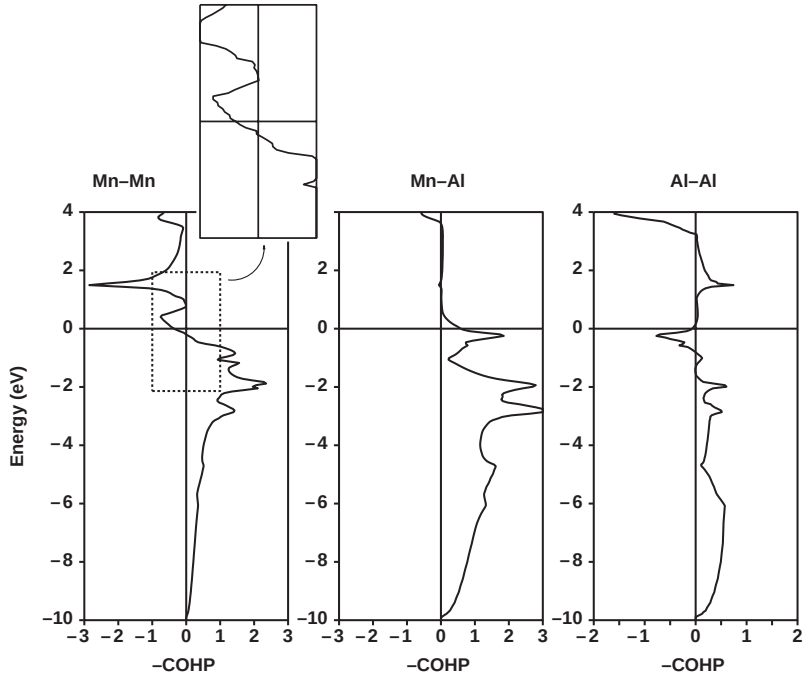

Fig. 5. Crystal orbital Hamilton population (COHP) curves for nonmagnetic cubic MnAl: The left plot represents the six nearest-neighbor Mn–Mn interactions (octahedral coordination) while the middle and right plots show the nearest Mn–Al (eightfold coordination) and Al–Al interactions (octahedral coordination), respectively.

point towards an underlying electronic instability. We have recently shown that spontaneous spin polarization may result in transition metals and their alloys [23] whenever antibonding M–M states at the Fermi level show up in nonmagnetic band structure calculations. Upon going magnetic, these antibonding states vanish, followed by strengthened covalent bonding for the elements, but not necessarily for intermetallic alloys.

Thus, spontaneous spin polarization is very much indicated for cubic MnAl. A similar hint is given by the course of the chemical hardness η as a function of the c/a axis ratio, extracted from TB-LMTO-ASA calculations in Fig. 6. All values are around (or even below) 0.2 eV, and the significantly smaller values at $c/a \approx 1.3$ even call for a further structural deformation.

In the following, we switched to a spin-polarized description of the electronic structure by means of the local spin density approximation (LSDA) but still keeped with the primitive cubic structure. As it turns out, the total energies are *significantly* lower, and the

Table 1
Integrated COHPs (ICOHPs) per bond for the different interactions in cubic and tetragonal MnAl on the basis of TB-LMTO-ASA calculations

	Mn–Mn 6 bonds (eV)	Mn–Al 8 bonds (eV)	Al–Al 6 bonds (eV)	E_{tot} (eV)
Cubic, nonmagnetic (LDA)	−5.71	−11.38	−2.71	0.0
Cubic, magnetic (LSDA)	−5.58 (α: −2.44 β: −3.14)	−11.30 (α: −5.36 β: −5.94)	−2.80 (α: −1.37 β: −1.43)	−0.243 (relative to cubic LDA)
Tetragonal, magnetic (LSDA)	−6.08 (α: −2.51 β: −3.57)	−10.59 (α: −4.97 β: −5.62)	−3.53 (α: −1.70 β: −1.83)	−0.290 (relative to cubic LDA)

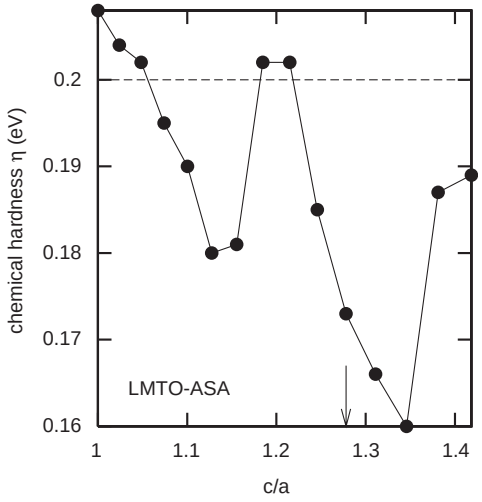

Fig. 6. The chemical hardness of nonmagnetic MnAl as a function of the axial ratio c/a. The arrow indicates the ratio of the real structure.

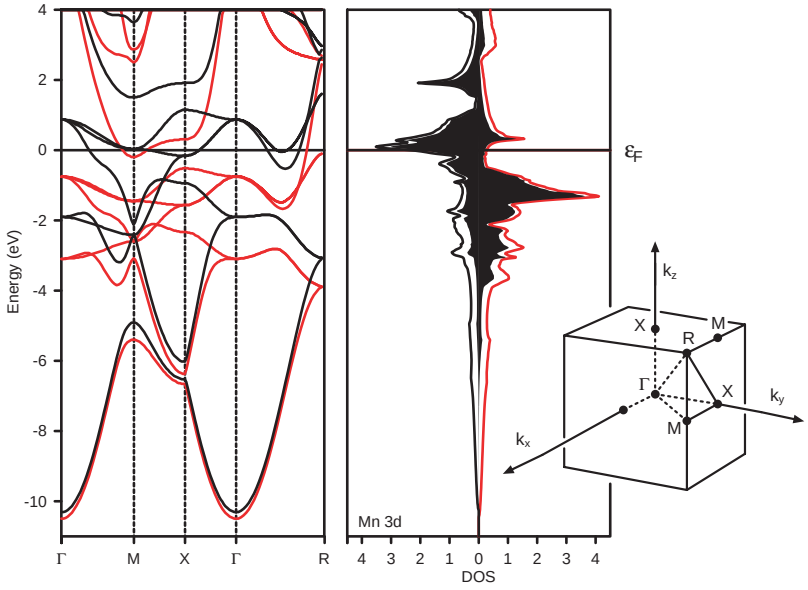

Fig. 7. TB-LMTO-ASA band structure (left) and density of states (right) of ferromagnetic MnAl in the cubic structure. In both plots, the red/black line corresponds to the α/β spins. All curves have been shifted in energy so that ε_F, indicated with the horizontal line, lies at 0.0 eV. The corresponding first Brillouin zone of a simple cubic lattice is included on the right.

stabilization is 0.243 eV (TB-LMTO-ASA) and 0.393 eV (FLAPW), resulting from the different occupations of the α and β spin sublattice which is 1.94 μ_B (TB-LMTO-ASA) and 1.85 μ_B (FLAPW), respectively. The LMTO atomic charges barely decrease to $-0.190/+0.190$ for Mn/Al.

The corresponding band structure and DOS plots, on the basis of the LMTO calculations, are presented in Fig. 7. As expected, the exchange splitting between the majority α (red) and minority β (black) levels is small for the 4*s* functions and much larger (1–2 eV) for the 3*d* bands such that most of the π bands belonging to the β spins have been emptied because of lying above ε_F. This shift in the *d* states is even more pronounced in the DOS plot; both spin-resolved DOSs, however, still resemble the nonmagnetic DOS (Fig. 3).

The COHP analysis (Fig. 8) of the interatomic bonding within this magnetic cubic phase fulfills our expectations. Al–Al bonding is almost untouched, and Mn–Al bonding changes somewhat due to the varied local electronic structure of the manganese atom (compare with Fig. 5). Mn–Mn bonding, however, is characterized by the removal of antibonding interactions at ε_F due to the repopulated spin sublattices. Table 1 furthermore shows that only the covalent part of the Al–Al bonding has slightly increased; the covalent

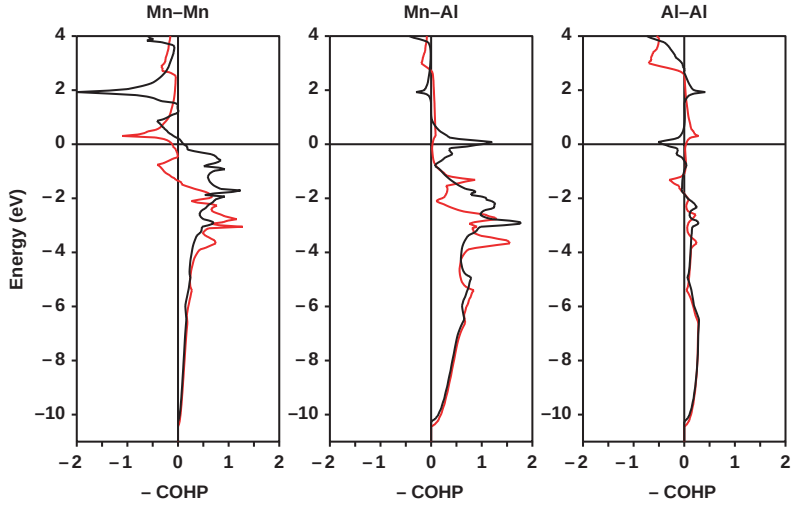

Fig. 8. Crystal orbital Hamilton population (COHP) curves for ferromagnetic cubic MnAl: The left plot represents the six nearest-neighbor Mn–Mn interactions (octahedral coordination) while the middle and right plots show the nearest Mn–Al (eightfold coordination) and Al–Al interactions (octahedral coordination), respectively. In each plot, the red/black line corresponds to the α/β spins. All curves have been shifted in energy so that ε_F, indicated with the horizontal line, lies at 0.0 eV.

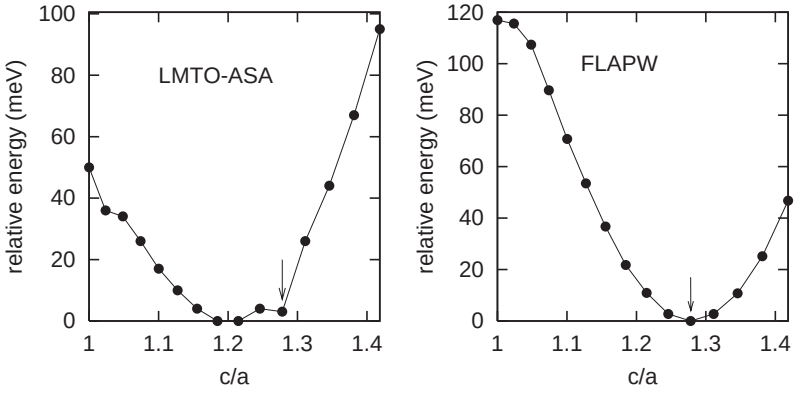

Fig. 9. The total energy of the TB-LMTO-ASA (left) and FLAPW (right) magnetic LSDA calculations as a function of the axial ratio c/a. The arrows indicate the ratio of the real structure.

bond strengths of Mn–Mn and Mn–Al have both decreased a little. This finding, together with the still antibonding nature of Al–Al bonding at ε_F, indicates that the electronic structure of magnetic cubic MnAl still can be further optimized. It is clear that an even stronger electronic distortion (increased magnetic moment) is seemingly impossible because of the insufficient intra-atomic exchange of the aluminum atom so that only structural changes are to be sought for.

We have therefore repeated the above-mentioned total energy calculations as a function of the c/a axis ratio for the magnetic case utilizing both TB-LMTO-ASA and FLAPW methods; their results have been plotted into Fig. 9. While there are significant numerical differences between the two approaches, both of them fully agree concerning the result in that a tetragonal structure with $c/a \approx 1.2$ (TB-LMTO-ASA) and $c/a \approx 1.3$ (FLAPW) is prefered. We also find a continuous decrease in Mn/Al atomic charges (LMTO) upon going tetragonal, e.g., $-0.177/+0.177$ for the experimental lattice parameters ($c/a = 1.28$). Although the more accurate full-potential LAPW approach correctly hits the latter ratio, we stick to the results of the simpler TB-LMTO-ASA method because of its easier interpretability.

The energetic gain by becoming tetragonal ($c/a = 1.28$) is an additional 0.047 eV (TB-LMTO-ASA) and 0.117 (FLAPW), indicating strong magneto-elastic coupling. The magnetic moments arrive at 2.32 μ_B (TB-LMTO-ASA) and 2.23 μ_B (FLAPW). The corresponding band structure and DOS diagram of the LMTO calculation is given in Fig. 10. While the increased complexity of the bands makes a simple understanding admittedly difficult (see also the appendix), it is obvious from the DOS that, surprisingly, the structural distortion has pushed the π-bonding part of

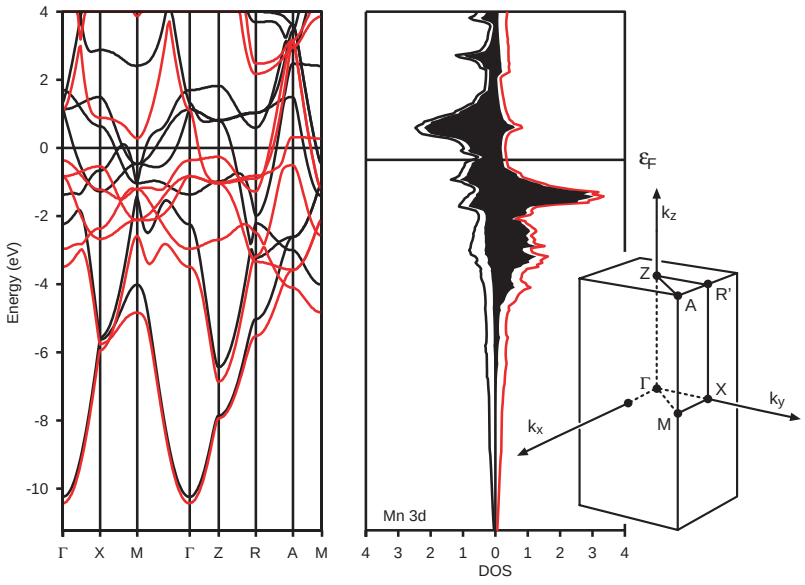

Fig. 10. TB-LMTO-ASA band structure (left) and density of states (DOS) of ferromagnetic MnAl in the tetragonal structure. In both plots, the red/black line corresponds to the α/β spins. All curves have been shifted in energy so that ε_F, indicated with the horizontal line, lies at 0.0 eV. The corresponding first Brillouin zone of a simple tetragonal lattice is included on the right.

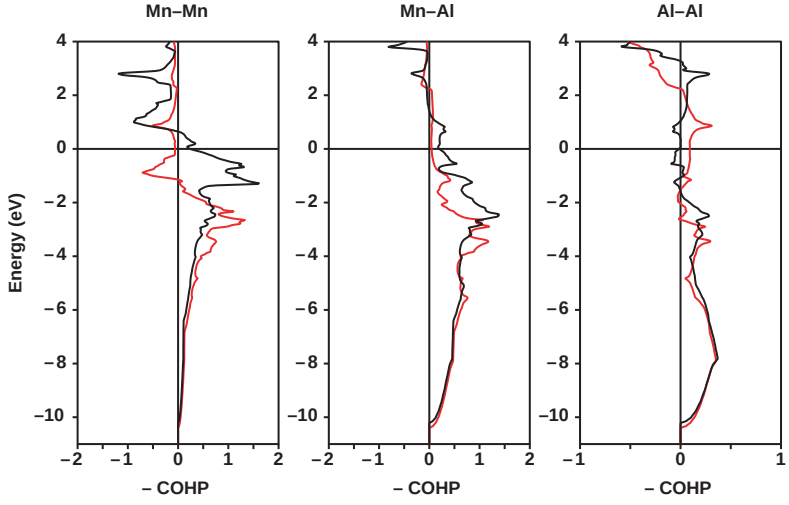

Fig. 11. Crystal orbital Hamilton population (COHP) curves for ferromagnetic tetragonal MnAl: Shown are the Mn–Mn interactions (left) for the six neighbors (four nearest and two next-nearest), the Mn–Al interactions (middle) for the eight nearest neighbors and the Al–Al interactions (right) for the six nearest and next-nearest neighbors. In each plot, the red/black line corresponds to the α/β spins. All curves have been shifted in energy so that ε_F, indicated with the horizontal line, lies at 0.0 e.V.

the β spins even more above the Fermi level, namely to ca. +0.8 eV; these were originally touching the Fermi level and centered at around +0.3 eV (see Fig. 7).

These results find their expression in the newly calculated COHPs (Fig. 11) for the tetragonal structure, to be compared with their cubic counterparts (Fig. 8). We mention that because of the tetragonal distortion we now have shorter and longer bonds for the Mn–Mn, Mn–Al, and Al–Al combinations (see Table 2); for reasons of simplicity, we still represent them by a single, averaged COHP curve for each interaction. In combination with the numerical values from Table 1, it is obvious that both Mn–Mn and Al–Al bonds have significantly strengthened, namely by 6.5% (Mn–Mn) and 30.3% (Al–Al) when compared to the nonmagnetic cubic structure. The formerly antibonding Al–Al states at ε_F (Fig. 8, cubic structure) have been totally removed by the symmetry reduction. The covalent part of the Mn–Al bonds, however, has been weakened throughout the entire process, namely by 6.3% when compared to the magnetic cubic and by 6.9% when compared to the nonmagnetic cubic crystal structure.

We are tempted to interpret the strengthening of the homoatomic (Mn–Mn, Al–Al) bonding and the weak-

Table 2
Interatomic distances (Å) in cubic and tetragonal MnAl

	Mn–Mn	Mn–Al	Al–Al
Cubic	6×3.006	8×2.604	6×3.006
Tetragonal	4×2.770	8×2.640	4×2.770
	2×3.540		2×3.540

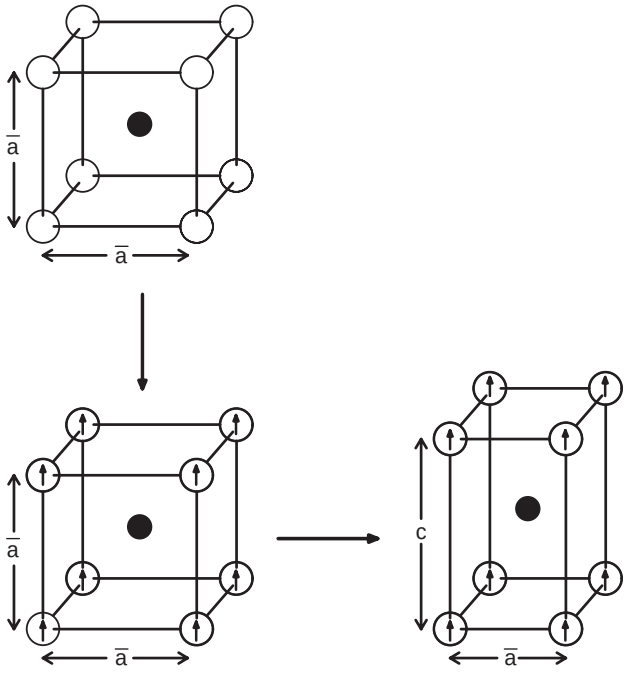

Fig. 12. Sequence of the distortion from nonmagnetic cubic MnAl to ferromagnetic tetragonal MnAl.

ening of the heteroatomic (Mn–Al) bonding as an electronic signpost for the beginning phase separation into elemental Mn and Al. In fact, τ-MnAl is reported to be only metastable.

4. Conclusion

The crystal structure of ferromagnetic tetragonal τ-MnAl may be understood to originate from the structure of nonmagnetic cubic MnAl with a CsCl motif through a two-step process. While the nonmagnetic cubic structure is *stable* against a structural deformation, antibonding Mn–Mn interactions at the Fermi level lead to spin polarization and the onset of magnetism, i.e., a *symmetry reduction taking place solely in the electronic degrees of freedom*, by that emptying antibonding Mn–Mn states. Residual antibonding Al–Al states can only be removed by a subsequent, energetically smaller *structural deformation towards the tetragonal system*; the process as a whole is schematically sketched in Fig. 12. As a final result, homonuclear bonding is strengthened and heteronuclear bonding is weakened.

Table 3
Symmetry points of the first Brillouin zone corresponding to the cubic and tetragonal unit cells

Simple cubic	Simple tetragonal	Relationship
Γ	Γ	Equivalent
X	X	Corresponding
M	M	Corresponding
X	Z	Broken degeneracy
M	R′	Broken degeneracy
R	A	Broken degeneracy

Acknowledgments

It is a pleasure to thank the *Deutsche Forschungsgemeinschaft* as well as the *Fonds der Chemischen Industrie* for their support.

Appendix

The structural distortion from ferromagnetic cubic MnAl to ferromagnetic tetragonal MnAl is mirrored by the different courses and dispersions of the spin-polarized bands depicted in Figs. 7 and 10. A direct comparison between these two figures, however, is complicated by the fact that the two band structures are plotted with respect to two different Brillouin zones, also given before in Figs. 7 and 10. In order to directly compare the spin-polarized cubic with the spin-polarized tetragonal bands, we have to plot the bands of ferromagnetic cubic MnAl in terms of a tetragonal representation.

The first Brillouin zone of the simple cubic lattice is a cube (Fig. 7, right), and the typical high-symmetry points have been indicated. In harmony with point group O_h, the d orbitals split into a doubly degenerate (e_g) and a triply degenerate (t_{2g}) set (see also Fig. 4). For a simple tetragonal structure, the first Brillouin zone is a cuboid (Fig. 10, right), and point group D_{4h} calls for a splitting of the d orbitals into three nondegenerate ones (a_{1g}, b_{1g}, b_{2g}) and one doubly degenerate (e_g) set. Taking into account the relationship between the special points of the two Brillouin zones given in Table 3, we expect the cubic e_g-set of orbitals to split into two tetragonal nondegenerate sets, and the cubic t_{2g} orbitals will change into a set of two doubly degenerate orbitals and one nondegenerate orbital upon tetragonal distortion. This is a consequence of the cubic high-symmetry point **X** corresponding to the tetragonal high-symmetry points

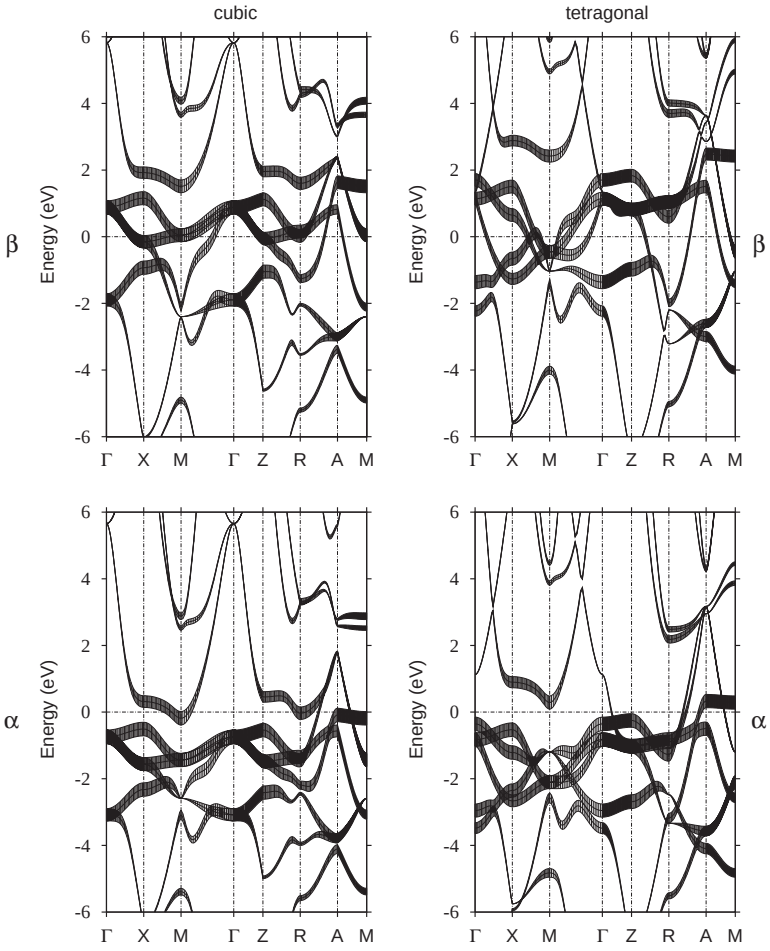

Fig. 13. Magnetic fatband representation of the Mn d bands in cubic (left) and tetragonal (right) MnAl, with minority (β) spins at the top and majority (α) spins at the bottom.

X and **Z**; likewise, cubic **M** changes into tetragonal **M** and **R**′.

Based upon this symmetry-related information, Fig. 13 presents the spin-polarized band structure of both cubic and tetragonal MnAl in terms of the same tetragonal Brillouin zone. In addition, the two spin sublattices are plotted separately, and the contribution of the Mn d orbitals to the bands is visualized by the bands's thicknesses, i.e., we offer a so-called *fatband* representation.

As has been said before, the three-above-two d splitting at the cubic **Γ** point changes into a one-above-two-above-one-above-one d splitting at tetragonal **Γ**. Also, the dispersion of the lower orbitals with σ interactions (cubic e_g set) is significantly stronger than those of the higher-lying π orbitals, and the dispersion is largest between **Γ**→**X** and **Γ**→**Z**. Upon tetragonal distortion, there are finer details: In particular, the cubic α spin band close to ε_F between **X** and **M** (Mn $d_{x^2-y^2}$ in character) becomes destabilized whereas the corresponding spin band between **Z** and **R**, also close to ε_F and Mn d_{z^2} in character, stabilizes a lot and dives into the valence band at ca. −1 eV. With respect to the minority β spin sublattice, the cubic spin band between **Γ**→**X** just above ε_F is also significantly stabilized upon distortion whereas the formerly occupied spin band between **Z** and **R** and **R** and **A** (around −1.5 up to 0 eV) becomes stabilized, too, but only after losing its former manganese d character.

Generally speaking, the β spin bands are much more affected by the cubic/tetragonal distortion. This effect goes back to the exchange hole, making the α/β spins experience an increased/lowered nuclear potential. Thus, the β spin orbitals tend to be more diffuse and are much stronger involved in the chemical bonding. The phenomenon can be recognized from a comparison of all β (top) and α (bottom) dispersions in Fig. 13, especially for the t_{2g}/e_g splitting at **Γ** in the cubic phase. It is also reflected by the α/β ICOHP values presented earlier in Table 1. A corresponding visualization of the same effect for α-Fe has been presented before using scaled electron density plots [23].

References

[1] A.J. McAlister, J.L. Murray, in: T.B. Massalski, H. Okamoto, P.R. Subramanian, L. Kacprzak (Eds.), Binary Alloy Phase Diagrams, American Society for Metals, Metals Park, OH, 1990.
[2] H. Kono, J. Phys. Soc. Jpn. 13 (12) (1948) 275.
[3] A.J.J. Koch, P. Hokkeling, M.G. van den Steeg, K.J. De Vos, J. Appl. Phys. 31 (1960) S75.
[4] P.B. Braun, J.A. Goedkoop, Acta Crystallogr. 16 (1963) 737.
[5] D.C. Crew, P.G. McCormick, R. Street, Scr. Metall. Material 32 (1995) 315.
[6] J.J. van den Brock, H. Donkersloot, G. van Tendeloo, J. van Landuyt, Acta Metall. 27 (1979) 1497.
[7] S. Kohima, T. Ohtani, N. Kato, K. Kojima, Y. Sakamoto, I. Konno, M. Tsukahara, T. Kubo, AIP Conf. Proc. 24 (1974) 768.
[8] A. Sakuma, J. Phys. Soc. Jpn. 63 (1994) 1422.
[9] O.K. Andersen, Phys. Rev. B 12 (1975) 3060.
[10] H. Skriver, The LMTO Method, Springer, Berlin, 1984.
[11] O.K. Andersen, in: P. Phariseau, W.M. Temmerman (Eds.), The Electronic Structure of Complex Systems, Plenum, New York, 1984.
[12] O.K. Andersen, O. Jepsen, Phys. Rev. Lett. 53 (1984) 2571.
[13] J. Korringa, Physica 13 (1947) 392.
[14] W. Kohn, N. Rostoker, Phys. Rev. 94 (1954) 1111.
[15] G. Krier, O. Jepsen, A. Burkhardt, O.K. Andersen, The TB-LMTO-ASA program, version 4.7, Max-Planck-Institut für Festkörperforschung, Stuttgart, Germany.
[16] U. von Barth, L. Hedin, J. Phys. C 5 (1972) 1629.
[17] P. Blaha, K. Schwarz, P. Sorantin, S.B. Trickey, Comput. Phys. Commun. 59 (1990) 399.
[18] J.P. Perdew, S. Burke, M. Ernzerhof, Phys. Rev. B 45 (1996) 3865.
[19] P. Blaha, K. Schwarz, J. Luitz, WIEN97, Vienna University of Technology 1997. (Improved and updated Unix version of the original copyrighted WIEN code [17].)
[20] R. Dronskowski, P.E. Blöchl, J. Phys. Chem 97 (1993) 8617, see also http://www.cohp.de.
[21] T. Hughbanks, R. Hoffmann, J. Am. Chem. Soc. 105 (1983) 3528.
[22] R. Hoffmann, Solids and Surfaces: A Chemist's View of Bonding in Extended Structures, VCH, Weinheim, 1988.
[23] R. Dronskowski, G.A. Landrum, Angew. Chem. Int. Ed. 39 (2000) 1560.
[24] A. Decker, G.A. Landrum, R. Dronskowski, Z. Anorg. Allg. Chem. 628 (2002) 303.
[25] R. Dronskowski, K. Korczak, H. Lueken, W. Jung, Angew. Chem. Int. Ed. 41 (2002) 2528.
[26] R.G. Pearson, Chemical Hardness, Wiley-VCH, Weinheim, 1997.